

Axisymmetric propagating vortices in centrifugally stable Taylor–Couette flow

C. Hoffmann¹, S. Altmeyer^{1,3}, M. Heise^{2,†}, J. Abshagen² and G. Pfister²

¹Institut für Theoretische Physik, Universität des Saarlandes, D-66123 Saarbrücken, Germany

²Institut für Experimentelle und Angewandte Physik, Universität Kiel, D-24098 Kiel, Germany

³Department of Mathematics, Kyungpook National University, Deagu, 702-701, Korea

(Received 11 January 2013; revised 5 April 2013; accepted 28 May 2013;
first published online 11 July 2013)

We present numerical as well as experimental results of axisymmetric, axially propagating vortices appearing in counter-rotating Taylor–Couette flow below the centrifugal instability threshold of circular Couette flow without additional externally imposed forces. These propagating vortices are periodically generated by the shear flow near the Ekman cells that are induced by the non-rotating end walls. These axisymmetric vortices propagate into the bulk towards mid-height, where they get annihilated by rotating, non-propagating defects. These propagating structures appear via a supercritical Hopf bifurcation from axisymmetric, steady vortices, which have been discovered recently in centrifugally stable counter-rotating Taylor–Couette flow (Abshagen *et al.*, *Phys. Fluids*, vol. 22, 2010, 021702). In the nonlinear regime of the Hopf bifurcation, contributions of non-axisymmetric modes also appear.

Key words: bifurcation, convection, nonlinear dynamical systems, pattern formation, Taylor–Couette flow

1. Introduction

Steady and time-dependent solutions of a fluid dynamical system provide the building blocks underlying the complexity in disordered or turbulent flows (Guckenheimer & Holmes 1983; Cross & Hohenberg 1993). In certain classes of hydrodynamically unstable systems, the structure of solutions and the organizing principles of complexity can be unfolded in a bifurcation analysis, such as in Rayleigh–Bénard convection (Bodenschatz, Pesch & Ahlers 2000) and in Taylor–Couette flow. The Taylor–Couette system consists of a viscous fluid between two independently rotating cylinders, and is one of the most famous references for pattern-forming systems. Numerous structures with different topology are known to appear in this system and have been studied extensively during the past decades. Experiments as well as numerical simulations (Di Prima & Swinney 1981; Andereck, Liu & Swinney 1986; Langford *et al.* 1988; Tagg 1994; Hoffmann & Lücke 2000; Marques & Lopez 2000; Lopez & Marques 2002; Hoffmann, Lücke & Pinter 2005; Heise *et al.* 2008; Hoffmann *et al.* 2009; Altmeyer & Hoffmann 2010) have elucidated various solutions and bifurcation scenarios.

† Email address for correspondence: heise@physik.uni-kiel.de

The simple geometries of the Taylor–Couette system leave the basic laminar flow invariant under certain symmetries, which determine the bifurcation behaviour (Golubitsky, Stewart & Schaeffer 1988; Cliffe, Mullin & Schaeffer 2012). Under axially periodic boundary conditions (PBCs) or in an infinite Taylor–Couette system, rotationally symmetric Taylor vortex flow (TVF) with toroidally closed vortices and spiral vortex flow (SPI; Tagg 1994; Hoffmann & Lücke 2000) with open, helical vortices bifurcating out of the basic state, i.e. circular Couette flow (CCF; Tagg 1994) can occur. For counter-rotating cylinders, non-axisymmetric spirals also occur from a centrifugal instability via a symmetry-breaking Hopf bifurcation. They are symmetry-degenerated in oppositely travelling, right-winding (R-SPI) or left-winding (L-SPI) spirals, which are mirror images of each other (Hoffmann & Lücke 2000; Hoffmann, Lücke & Pinter 2004). In the centrifugally stable regime between counter-rotating cylinders, even turbulent flow can appear directly out of the basic laminar flow as a consequence of a subcritical transition (Coles 1965; Borrero-Echeverry, Schatz & Tagg 2010).

In experimental realizations of Taylor–Couette flow, the viscous fluid is often enclosed by non-rotating axial end walls (e.g. non-rotating lids) at top and bottom, and therefore the axial translation invariance is broken. Furthermore, these end walls generate disturbances at any driving rate (Benjamin 1978; Edwards, Beane & Varma 1991; Czarny *et al.* 2003; Altmeyer *et al.* 2010), generating axisymmetric, secondary circulation. These so-called Ekman vortices overlay and deform the CCF and create a new stationary, rotationally symmetric basic flow. This state always contributes to the axial Fourier spectra of other flow states (stronger in short systems), and the bifurcation behaviour of Taylor vortices and spirals is significantly altered (Benjamin 1978; Lorenzen, Pfister & Mullin 1983; Edwards *et al.* 1991; Tagg 1994; Lopez, Marquez & Shen 2000; Czarny *et al.* 2003; Altmeyer *et al.* 2010; Cliffe *et al.* 2012).

In enclosed Taylor–Couette flow, a large variety of solutions have been discovered in the centrifugally stable regime. Localized and global spiral vortices have been found to bifurcate via a supercritical Hopf bifurcation out of the basic flow in counter-rotating flows (Avila *et al.* 2008; Heise *et al.* 2013) as well as in co-rotating flows (Heise *et al.* 2008) at critical Reynolds numbers and below that of the centrifugal instability of CCF, respectively. Axisymmetric cellular states, i.e. toroidally closed non-propagating n -vortex (nV) states with different numbers n of cells, have been observed in the centrifugally stable regime of counter-rotating Taylor–Couette flow. While these steady states appear smoothly in the basic flow, they give rise to a considerable multiplicity of states. This has been attributed to the homoclinic snaking mechanism (Abshagen *et al.* 2010).

In this paper, we report numerical and experimental results of axisymmetric *propagating* vortices (pV) that bifurcate in a supercritical Hopf bifurcation out of the *stationary* cellular (nV) states (Abshagen *et al.* 2010). The critical points of pV are located in the centrifugally stable regime of counter-rotating Taylor–Couette flow. In contrast to propagating spiral vortices, which are non-axisymmetric rotating waves, these axisymmetric propagating vortices are time-dependent in any rotating frame and reflection symmetry is revealed.

2. System

In our Taylor–Couette system, a Newtonian fluid of kinematic viscosity ν fills the annular gap between two concentric, independently rotating cylinders (inner, outer radii $r_{1,2}$; angular velocities $\Omega_{1,2}$). Throughout this paper, we consider a fixed radius

ratio of $\eta = r_1/r_2 = 0.5$. The system length Γ is given in units of the gap width $d = r_2 - r_1$, and rigid, non-rotating lids close the gap and serve as end walls in the axial direction.

Owing to the geometry of the system, cylindrical coordinates r, φ, z are used to decompose the velocity field into a radial component u , an azimuthal one v , and an axial one w :

$$\mathbf{u} = u \mathbf{e}_r + v \mathbf{e}_\varphi + w \mathbf{e}_z. \quad (2.1)$$

Lengths are scaled by the gap width $d = r_2 - r_1$, multiplied by the radial diffusion time d^2/ν for momentum across the gap, and the pressure is scaled p by $\rho\nu^2/d^2$. The Reynolds numbers

$$R_1 = r_1\Omega_1 d/\nu, \quad R_2 = r_2\Omega_2 d/\nu, \quad (2.2)$$

enter into the boundary conditions for v : here R_1 and R_2 are just the reduced azimuthal velocities of the fluid at the cylinder surfaces.

2.1. Numerical methods

The system is governed by the Navier–Stokes equations

$$\partial_t \mathbf{u} = \nabla^2 \mathbf{u} - (\mathbf{u} \cdot \nabla) \mathbf{u} - \nabla p. \quad (2.3)$$

For numerical simulations, we used a G1D3 code developed by Hoffmann and extensively described in Hoffmann *et al.* (2004). It is a combination of a finite differences method in time, radial and axial directions, and a Galerkin expansion in φ direction, with a decomposition

$$f(r, \varphi, z, t) = \sum_m f_m(r, z, t) e^{im\varphi}, \quad (2.4)$$

where f denotes one of $\{u, v, w, p\}$. As in Hoffmann *et al.* (2004), we choose a sufficiently large Fourier mode space with $m_{max} = 8$ for an adequate accuracy.

For the flows investigated here, a truncation of the Fourier expansion at $m_{max} = 8$ has been verified to properly resolve the anharmonicities in the fields. Deeper investigations have shown that the (cylindrical) system always prefers structures with smaller azimuthal wavenumbers m . This also holds for the subcritical case, where $m \neq 0$ modes (originating from fluctuations) are excited by $m = 0$ modes (originating from the end walls) through nonlinearities (cf. Altmeyer *et al.* (2010) for the interaction of $m = 0$ and $m \neq 0$ structures).

For code validation, we compared travelling and non-travelling solutions within a wide range of wavenumbers with experiments (e.g. Heise *et al.* 2008) and previous numerical results. We also investigated how the nonlinear solutions change when varying m_{max} and/or the grid spacing. From these analyses, we conservatively conclude that typical spiral frequencies have an error of less than $\sim 0.2\%$, and that typical velocity field amplitudes of non-propagating vortices can be off by significantly less than 3–4%. Time steps were always well below the von Neumann stability criterion and by more than a factor of three below the Courant–Friedrichs–Lewy criterion. We found an error depending on the variation of time steps to lie below 1%. Higher radial and axial resolutions nor higher maximal azimuthal mode numbers lead to a significantly improved accuracy of the observed structures.

For diagnostic purposes, we also calculate the complex mode amplitudes $f_{m,n}(r, t)$ representing the Fourier decomposition in the axial direction

$$f_m(r, z, t) = \sum_n f_{m,n}(r, t) e^{inkz} \quad (2.5)$$

of numerically obtained fields $f_m(r, z, t)$. Besides this, we also used a shooting method in order to calculate linear stability thresholds (Altmeyer, Hoffmann & Lücke 2011).

For flow visualization, it was shown that the azimuthal vorticity component

$$\Omega_\varphi = \partial_z u - \partial_r w \quad (2.6)$$

is an adequate and convenient means to identify and recognize the geometry of complex vortex structures via isovorticity surfaces (Hoffmann *et al.* 2009). The tubes obtained in this way represent the topology of vortex centres and thus determine the most important properties of the structures, e.g. symmetry and connectivity. Moreover, they describe the strength of the vortices and give a rough impression of the vortex deformation. Light grey (green online) and dark grey (red online) shading of Ω_φ corresponds to vortex rotation in the negative and positive mathematical directions, respectively, while looking towards the positive azimuthal direction.

2.2. Experimental set-up

In our experiments, the temperature of the fluid is thermostatically controlled at 24.00 ± 0.01 °C. The inner cylinder of our apparatus is machined from stainless steel having a radius of $r_1 = 12.50 \pm 0.01$ mm, while the outer cylinder is made from optically polished glass with a radius of $r_2 = 25.00 \pm 0.01$ mm. At the top and the bottom, the fluid is confined by solid end walls, and the tilt of each wall is better than 0.03 mm at the outer diameter. The rotation of the cylinders is controlled by a phase-locked loop (PLL) unit achieving an average accuracy of $\Delta f/f \propto 10^{-4}$ in the short term and $\Delta f/f \propto 10^{-7}$ in the long term. As a working fluid within the gap between the two concentric cylinders, a silicone oil with a kinematic viscosity $\nu = 9.6 \pm 0.1$ cSt is used. The uncertainty of ± 0.1 cSt refers to the measurement of the absolute value of the kinematic viscosity. The accuracy of ν during a measurement is primarily determined by the temperature variation of the fluid, which is thermostatically controlled to 24.00 ± 0.01 °C. This yields $\Delta \nu = (\partial \nu / \partial T)|_{24.00 \text{ °C}} \Delta T \approx 0.0025$ cSt. Though the uncertainty in the absolute value of ν introduces an uncertainty $\Delta R_{abs}/R \propto 10^{-2}$ in the absolute value of the Reynolds number R , the variation in the Reynolds number with time is within $\Delta R/R \propto 10^{-4}$ during a measurement. This variation determines the resolution in Reynolds numbers that is achieved in the experiment.

In addition to flow visualization, we utilize laser Doppler velocimetry (LDV) for measurements of the local radial and axial velocity of the flow. In this work, two different LDV measurement techniques are used. The first method measures the velocity component u or w at a fixed position (r, φ, z) . The second is an axial scan of u or w , moving the LDV with constant velocity in z at fixed r and φ . In order to study the complete spatio-temporal behaviour of the flow, sequential axial scans are performed for u and w .

3. Results

3.1. Stationary vortices

In figure 1, we use numerically determined isosurfaces of the azimuthal vorticity $\Omega_\varphi = \pm 60$ in order to visualize the ‘classical’ Ekman-dominated basic two-vortex

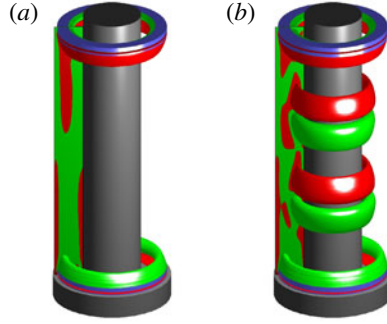


FIGURE 1. (Colour online) Isosurfaces of the azimuthal vorticity $\Omega_\varphi = \pm 60$ of numerically simulated flows for two different subcritical nV states: (a) subcritical 2V state with two Ekman vortices covering the whole system height; (b) another subcritical state (6V) consisting of two Ekman vortices and four small vortices near mid-height located close to the inner cylinder. The grey shades (colours online) for this and all subsequent figures showing isosurfaces are: dark grey (red online), $\Omega_\varphi = +60$; light grey (green online), $\Omega_\varphi = -60$. Control parameters are $R_2 = -300$ and $\Gamma = 4$ for both simulations; and $R_1 = 110$ in panel (a) and $R_1 = 150$ in panel (b).

state (2V) in panel (a) as well as a six-vortex state (6V) in panel (b) – cf. Heise *et al.* (2013). The two strong Ekman cells in figure 1(a) are located near the lids but dominate the flow in the whole gap, which is indicated by the sign of Ω_φ in the slice (dark grey/red online corresponds to positive, light grey/green online corresponds to negative Ω_φ). In the 6V state in figure 1(b), on the other hand, four extra vortices occur in addition to the Ekman vortices. They are symmetrically arranged around mid-height and mainly located close to the inner cylinder. The vortex number n and the axial wavelength of all these toroidally closed vortices depend on the axial length Γ and the aspect ratio η of the system (see Abshagen *et al.* (2010) for details).

3.2. Propagating vortices

In general, propagating states like spirals are quite common in co-rotating as well as in counter-rotating Taylor–Couette flow. However, the subcritical occurrence of the propagating vortices observed here, on the one hand, and the toroidally closed structure, on the other, makes them very interesting. Note that toroidally closed, *propagating* vortices have not been observed in a closed Taylor–Couette system (without externally imposed additional forces like magnetic fields or axial pressure gradients) so far. These propagating vortex (pV) states emerge out of different subcritical, stationary nV solutions, which are discussed above and shown in figure 1.

As an example, figure 2 depicts snapshots of a pV state. The sequence covers one period T and shows that new vortices are generated at the defects near the lids and are annihilated in a pair of defects near mid-height. The spatio-temporal dynamics of vortex generation and annihilation in this pV state can easily be followed in the sketch of figure 2(b), which describes the vortex generation, propagation and annihilation in the gap (we omitted the Ekman cells; left (right) edge correspond to inner (outer) cylinder).

We start our discussion at $t_1 = 0$ (1) in figure 2(b), when the pV state exhibits six vortices, i.e. two pairs of vortices in the bulk as well as two Ekman vortices (not shown in panel (b)) near the lids. In (2), two new vortex pairs (labelled 5/6 and 8/7), located between the bulk vortices (1/2 and 4/3) and the respective Ekman vortices,

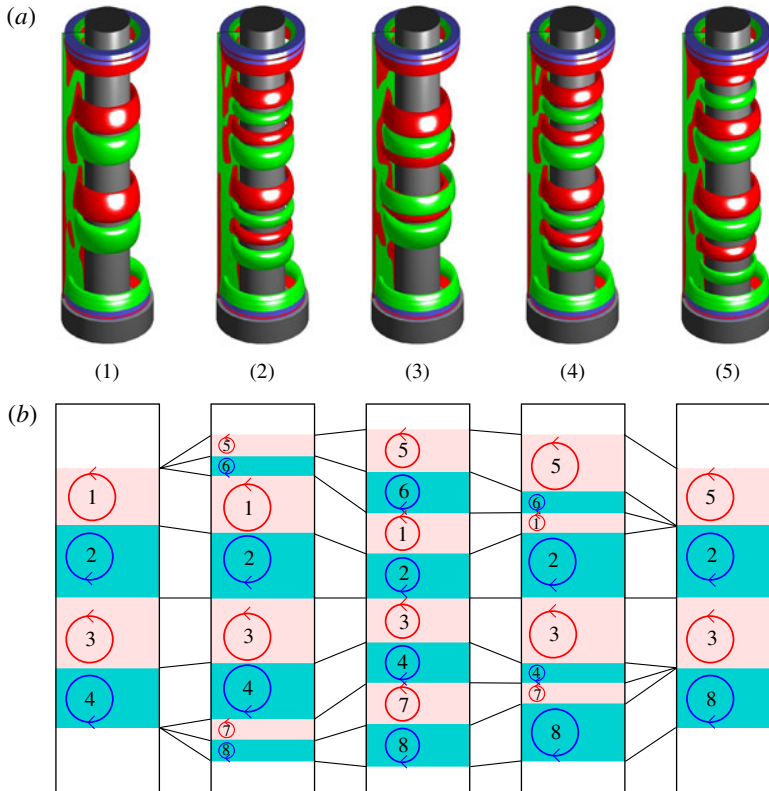


FIGURE 2. (Colour online) (a) Isosurfaces of the azimuthal vorticity ($\Omega_\varphi = \pm 60$) of numerically simulated flow states covering one characteristic period of a pV state for five different time positions $t_1 = 0$, $t_2 = 0.041$, $t_3 = 0.072$, $t_4 = 0.133$ and $t_5 = 0.195$. (b) Schematic illustration for the generation and annihilation of vortices in the gap between the inner (left edge) and outer (right edge) cylinder. The vortices are labelled by 1 to 8. Note that we removed the Ekman vortices for better visibility. Control parameters are $R_1 = 165$, $R_2 = -300$ and $\Gamma = 4$.

appear quite close to the inner cylinder. As a result of the larger number of vortices in the bulk, both vortex pairs (1/2 and 4/3) move together. The new vortex pairs (5/6 and 8/7) keep growing in axial and radial directions such that, in (3), all bulk vortices have nearly the same extension. Now, in (4), the inner vortex pairs (6/1 and 7/4) in each localized vortex domain become smaller to the benefit of the respective boundary vortices (5/2 and 8/3) and finally disappear in (5). The last state (5) after a complete period is again a pV state exhibiting six vortices, which is the initial state (1) of the periodic process. The period of vortex generation and annihilation here is $T \approx 0.19$ corresponding to a frequency $f \approx 5.05$. We found that this frequency does not vary significantly with R_1 or R_2 .

Additionally, figure 3 shows the zeros of the radial flow field in a space–time plot for a $\Gamma = 4$ system in panel (a) as well as a longer $\Gamma = 8$ -system in panel (b) and exhibits the propagation and dynamics of the pV state. The zeros of one velocity component correspond to defects, which are the origin of phase generation or annihilation.

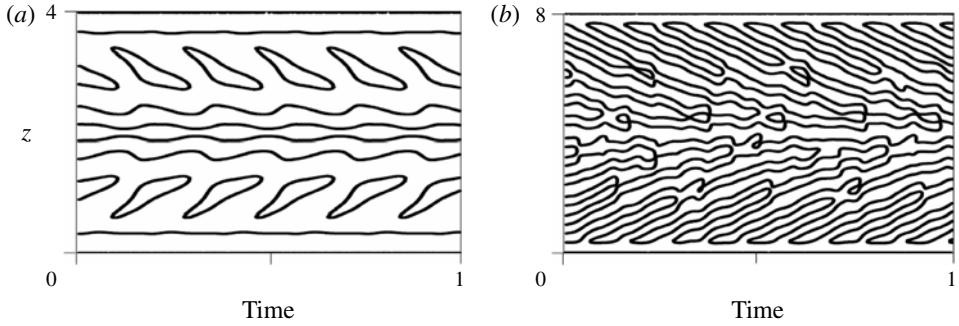


FIGURE 3. Space–time plots of the radial velocity $u = 0$ of numerically obtained pV states observed for two different axial lengths: (a) $\Gamma = 4$ and (b) $\Gamma = 8$. Further control parameters are $R_1 = 165$, $R_2 = -300$, $r = r_1 + 0.5$ in panel (a), and $R_1 = 225$, $R_2 = -600$, $r = r_1 + 0.25$ in panel (b).

Figures 2 and 3 exhibit two interesting aspects, which we want to point out: (i) the pV state consists of toroidally closed vortices with a dominant $m = 0$ azimuthal mode contribution; and (ii) the inner vortices (2, 3) lie between both vortex-annihilating defects and are therefore only affected as they periodically change their axial wavenumber.

3.3. Bifurcation scenario

In the following the transition from a stationary vortex nV flow state to a propagating pV state is discussed in detail. Therefore, we experimentally measured the axial velocity w by LDV at a fixed radial ($r = r_1 + 0.08$) and azimuthal φ position using axial scans along $z \in [0.15, 3.85]$. In order to measure the bifurcation, we quasi-statically increased R_1 after each axial scan at a fixed R_2 . We found the spatio-temporal average $\langle w \rangle_{z,t}^2$ of $w(r, \varphi, t)$ at the fixed radial and azimuthal position to provide a good measure for the transition points between non-propagating vortices (2V and 6V). In addition to that, we used the bandpass filtering method to distinguish between non-propagating vortices and propagating ones (see Heise *et al.* (2008) for details). In figure 4 the transitions from 2V to 6V and from 6V to pV are analysed by this method. Below the onset of 6V, $\langle w \rangle_{z,t}^2$ (\bullet) is found to increase linearly. The onset of cellular states is determined from the deviation from this linear growth by a nonlinear fitting method, as described in Abshagen *et al.* (2010). Based on this estimation, we determined the onset of 6V at $R_{1,c} = 150.5$ (vertical dashed line).

In order to estimate the critical value for the transition from 6V to pV, two further curves are depicted in figure 4. The w_{nV} curve (\circ) only considers non-propagating velocity components, whereas the w_{pV} curve (\square) illustrates the propagating ones. One can see that the pitch of the w_{nV} curve is reduced as the w_{pV} curve increases significantly at $R_{1,c} = 161.5$ (vertical dotted line). For the w_{pV} curve, $\langle w \rangle_{z,t}^2$ increases linearly for $R_1 > R_{1,c}$ as expected for a supercritical Hopf bifurcation.

In figure 5 two numerically determined bifurcation scenarios are depicted. The bifurcation diagram for rigid boundary conditions (RBCs; $\Gamma = 4$) in panel (a) and for axially periodic boundary conditions (PBCs) in panel (b). First, focusing on the RBC case, the stable 2V state in region A undergoes a smooth transition to a 6V state (region B), which becomes unstable against a pV state remaining stable all over the parameter regions C and C'. In C', pV and TVF (with eight vortices) coexist

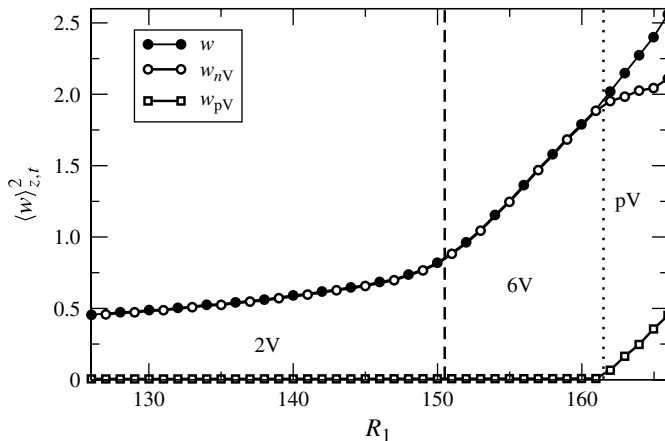


FIGURE 4. Experimentally determined bifurcation diagram measured at $R_2 = -380$ and $\Gamma = 4$, where the spatial mean of the squared axial velocity $\langle w \rangle_{z,t}^2$ and additionally the bandpass filtered curves of the non-propagating vortices w_{nV} as well as the propagating vortices w_{pV} are plotted versus R_1 . The vertical dashed and dotted lines indicate the critical stability boundaries of the flow states 2V, 6V and pV as indicated.

as bistable solutions. The latter undergoes a transition to the pV state at onset. All structures have significantly different wavenumbers k (mainly due to the variable number of vortices), which remain more or less constant within the respective regions A to C'. For the $\Gamma = 4$ system, we found $k = 3.9$ for 6V (six vortices), $k = 7.2$ for TVF (eight vortices) and $k = 5.7$ for pV (six to 10 vortices).

For comparison, figure 5(b) elucidates the bifurcation scenario for an axially periodic system by fixing the periodicity length to the respective wavenumber of the corresponding structure in panel (a). For the SPI state, which does not exist in the RBC system, we used the critical wavenumber $k = k_c$ of $m = 1$ solutions.

Owing to the absence of Ekman boundary layers as a driving force under PBC, *no* subcritical non-trivial structures are found at all. Even the supercritical pV state as observed in figure 5(a) is *missing* here. On the other hand, stable spirals occur in a very small region near onset, and the Taylor vortices bifurcate as an unstable solution to the benefit of stable wavy Taylor vortices (wTVF) (Hoffmann *et al.* 2009; Altmeyer *et al.* 2010), which are described by their significant $m = 0$ and $m = \pm 1$ modes.

3.4. Phase diagram

Figure 6 exhibits a combined experimentally measured and numerically simulated phase diagram for different subcritically and supercritically appearing vortex states in the counter-rotating regime. The dotted dark grey (blue online) and light grey (orange online) curves denote the well-known (critical) linear stability threshold for $m = 0$ and $m = 1$, respectively, distinguishing the supercritical from the subcritical CCF regime. In this figure, the experimentally (numerically) determined values are denoted by filled (open) symbols.

For small R_1 , one only observes the 2V state for all R_2 values depicted here. Depending on R_2 , it is replaced by either 4V or 6V states while increasing R_1 . The solid black line with circles (\circ, \bullet) characterizes the smooth transition from 2V to nV states ($n = 4, 6$) (see also Abshagen *et al.* (2010) for further details). The dashed line with diamonds (\diamond, \blacklozenge) gives the bifurcation threshold for pV states out of nV states.

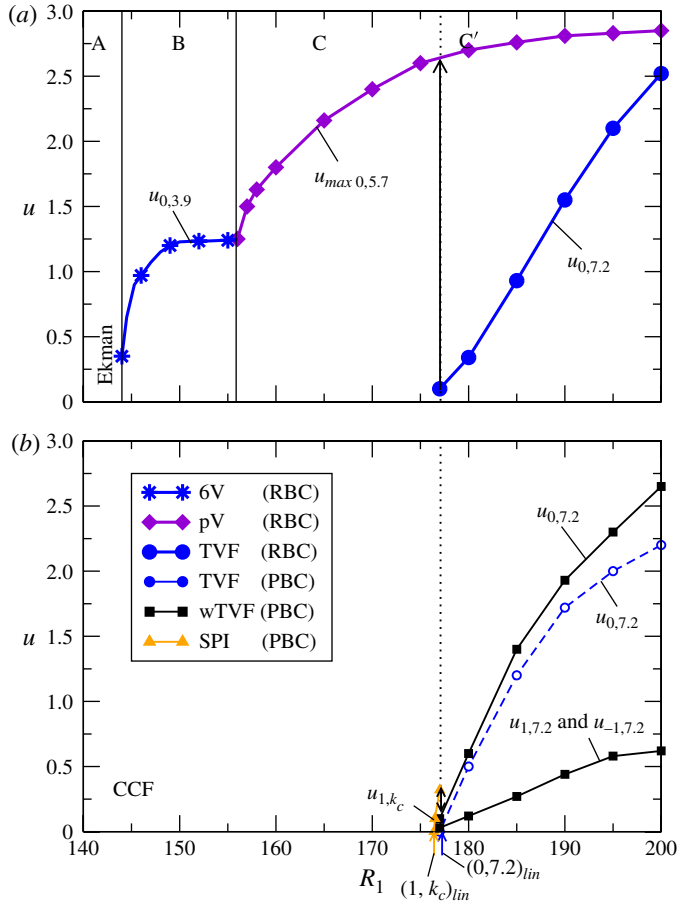


FIGURE 5. (Colour online) Numerically obtained bifurcation diagrams measured at $R_2 = -300$ and $\Gamma = 4$ of different subcritical and supercritical states 2V, 6V, pV, TVF, wTVF and SPI for (a) rigid boundary conditions (thick lines) as well as for (b) axially periodic boundary conditions (thin lines). The axial wavenumbers k of all structures are given as indices. Solid (dashed) lines with filled (open) symbols refer to stable (unstable) solutions. Shown are the dominant axial Fourier amplitudes $|u_{m,k}|$ of the azimuthal modes $|u_m(z)|$ (see equation (2.5)) of the radial flow $u(r, \varphi, z, t)$ at mid-gap and $z = 1$. In C and C', we chose the temporal maximum u_{max} of $u(r, \varphi, z, t)$ at a suitable fixed position ($r = r_1 + 0.5, \varphi = \text{const.}, z = 1$) for the pV state. Labels $m > 0$ and $m < 0$ refer to left- and right-winding azimuthal helical modes, respectively. The small dark grey (blue online) and light grey (orange online) arrows below the abscissa in panel (b) indicate the linear stability threshold of the $(m = 0, k = 7.2)$ and $(m = 1, k = k_c)$ solutions, respectively. Different regions are labelled by A (2V state), B (6V state), C (pV state) and C' (bistable pV and TVF state).

As discussed above, these pV states can occur supercritically out of nV states. For stronger counter-rotation, on the other hand, the nV regime ($n = 4, 6$) becomes more and more narrow but does not disappear completely in the regime depicted in figure 6.

3.5. Non-axisymmetric flow states

Non-axisymmetric flow states are also observed in the vicinity of the flow states presented above. In figure 7, a numerical simulation of such a flow state is illustrated

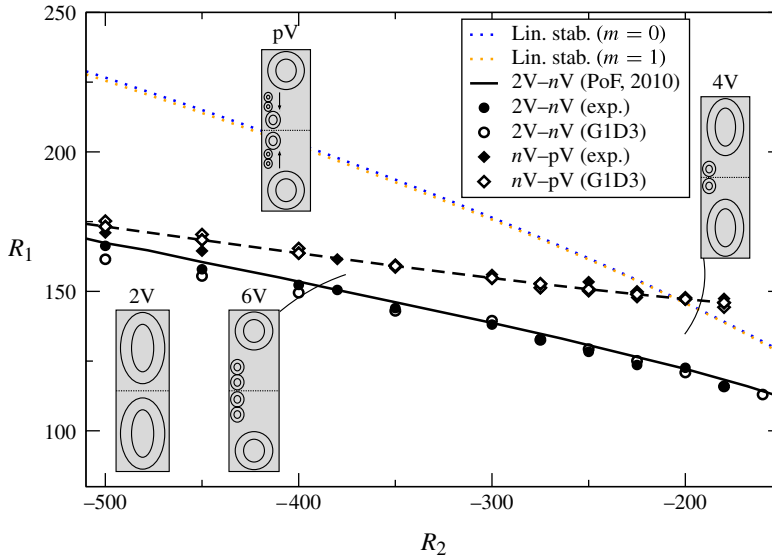


FIGURE 6. (Colour online) Numerically and experimentally obtained phase diagram in the R_1 - R_2 plane including the different onsets of nV states (4V and 6V) as well as pV states for $\Gamma = 4$. The dotted dark grey (blue online) and light grey (orange online) curves, respectively, denote the numerically determined linear stability threshold for critical $m = 0$ and $m = 1$ solutions out of CCF. The solid black line (from Abshagen *et al.* (2010)) with circles (\circ , \bullet) characterizes the smooth transition between different nV states, while the dashed line with diamonds (\diamond , \blacklozenge) gives the bifurcation threshold for pV states out of nV states. All experimentally (numerically) obtained values are indicated as filled (open) symbols. The four insets sketch these different solutions.

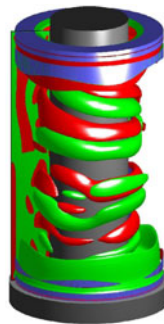


FIGURE 7. (Colour online) Isosurface of the azimuthal vorticity ($\Omega_\varphi = \pm 60$) of numerically simulated non-axisymmetric flow state. The $m \neq 0$ contributions to the state are clearly visible. Control parameters are $R_1 = 200$, $R_2 = -600$ and $\Gamma = 4$.

by the azimuthal vorticity ($\Omega_\varphi = \pm 60$). In contrast to the pV states presented above (e.g. figure 2), this state also includes $m \neq 0$ contributions. However, the vortices still *remain* toroidally closed, and the vortex generation and annihilation as well as the propagation are similar to those illustrated in figure 2, but the axial reflection symmetry is broken. In general, $m = 0$ modes are much stronger (compared to $m \neq 0$

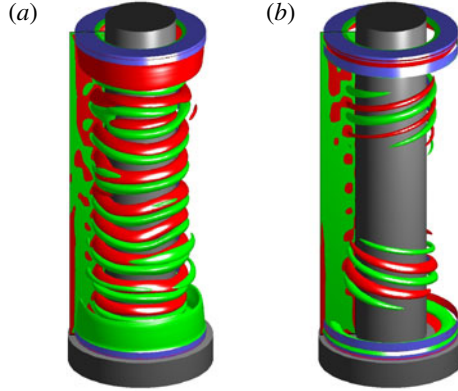


FIGURE 8. (Colour online) Isosurface of the azimuthal vorticity ($\Omega_\phi = \pm 60$) of two different numerically simulated non-axisymmetric flow states. (a) Flow state exhibiting many more vortices and visible $m \neq 0$ contributions. (b) Flow state with mainly helical ($m = \pm 1$) contributions. Control parameters are $\Gamma = 8$, $R_2 = -300$ and $R_1 = 174$ in panel (a) as well as $R_1 = 162$ in panel (b).

contributions) due to the greater influence of rotationally symmetric Ekman cells, which are generated by rotationally symmetric (non-rotating) lids.

After the above discussion of non-axisymmetric states in a $\Gamma = 4$ system, we now focus on the influence of increasing the system length Γ and the thereby decreasing the influence of Ekman-induced perturbations on bulk structures.

In general, we found that increasing the system length Γ leads to a strengthened contribution of helical $m \neq 0$ azimuthal modes to the mode spectrum, resulting in a much more wavy-like deformation of pV states (cf. figure 8(a) for $\Gamma = 8$). Apart from this vortex modulation, the spatio-temporal behaviour and the dynamics are similar to those of the smaller $\Gamma = 4$ system at higher counter-rotation. The processes of vortex generation and annihilation remains qualitatively unchanged from those presented in figure 2. However, owing to the axially enlarged bulk region, the number of vortices increases accompanied by larger axial wavenumbers. Moreover, vortices are located closer to the inner cylinder, which agrees with previous investigations of subcritical nV states (Abshagen *et al.* 2010). Note that the flattened Ekman ‘potential’ near mid-height leads to a more or less free displacement of the inner, non-propagating vortex pair.

Furthermore, figure 8(b) illustrates a subcritical spiral state whose shape is similar to that observed in the co-rotating system as described in (Heise *et al.* 2013). However, in the counter-rotating case depicted here, besides $m = \pm 1$ we found various other azimuthal wavenumbers $|m| \geq 2$. The flow state illustrated in figure 8(b) exhibits many more partly toroidally closed vortices showing $m \neq 0$ contributions.

4. Conclusions

We have analysed numerically as well as experimentally a novel type of axisymmetric flow state that exists in counter-rotating Taylor–Couette flow even below the centrifugal instability of circular Couette flow and without any additional externally imposed forces. In addition to different types of non-propagating vortex states

(so-called nV states (Abshagen *et al.* 2010)), we observed propagating vortex solutions with a toroidally closed topology (so called pV states).

In general, we obtained an excellent agreement between numerical and experimental results. Propagating as well as non-propagating vortex states are generated (driven by shear flow) at the Ekman layers near both end walls. The occurring non-propagating flow states are members of a large family of multi-stable states differing in the number n of vortices. These small, axisymmetric vortices are located close to the inner cylinder. For propagating flow states, the axisymmetric small vortices propagate towards mid-height and are always generated near the end walls. They generally bifurcate via a supercritical Hopf bifurcation out of nV and exist in a wide parameter range. Since Ekman cells are the driving force for the generation of pV and subcritical nV states, they do not exist under axially periodic boundary conditions.

Furthermore, also toroidally closed and propagating but *non-axisymmetric* structures appear for stronger counter-rotation and axially larger systems. These states can also break the axial reflection symmetry. The novel propagating vortices may interact with the non-propagating, axisymmetric states and give rise to complex dynamics in the centrifugally stable regime of counter-rotating Taylor–Couette flow.

Acknowledgements

We thank the Deutsche Forschungsgemeinschaft (AB336-1/2) for financial support and M. Lücke for fruitful discussions.

REFERENCES

- ABSHAGEN, J., HEISE, M., PFISTER, G. & MULLIN, T. 2010 Multiple localized states in centrifugally stable rotating flow. *Phys. Fluids* **22**, 021702.
- ALTMAYER, S. & HOFFMANN, C. 2010 Secondary bifurcation of mixed-cross-spirals connecting travelling wave solutions. *New J. Phys.* **12** (11), 113035.
- ALTMAYER, S., HOFFMANN, C., HEISE, M., ABSHAGEN, J., PINTER, A., LÜCKE, M. & PFISTER, G. 2010 End wall effects on the transitions between Taylor vortices and spiral vortices. *Phys. Rev. E* **81** (6), 066313.
- ALTMAYER, S., HOFFMANN, C. & LÜCKE, M. 2011 Islands of instability for growth of spiral vortices in the Taylor–Couette system with and without axial through flow. *Phys. Rev. E* **84** (4), 046308.
- ANDERECK, C. D., LIU, S. S. & SWINNEY, H. L. 1986 Flow regimes in a circular Couette system with independently rotating cylinders. *J. Fluid Mech.* **164**, 155–183.
- AVILA, M., GRIMES, M., LOPEZ, J. M. & MARQUES, F. 2008 Global endwall effects on centrifugally stable flows. *Phys. Fluids* **20**, 104104.
- BENJAMIN, T. B. 1978 Bifurcation phenomena in steady flows of a viscous fluid. I. Theory. – II. Experiments. *Proc. R. Soc. Lond. A* **359**, 1–26 and 27–43.
- BODENSCHATZ, E., PESCH, W. & AHLERS, G. 2000 Recent developments in Rayleigh–Bénard convection. *Annu. Rev. Fluid Mech.* **32** (1), 709–778.
- BORRERO-ECHEVERRY, D., SCHATZ, M. F. & TAGG, R. 2010 Transient turbulence in Taylor–Couette flow. *Phys. Rev. E* **81**, 025301.
- CLIFFE, K. A., MULLIN, T. & SCHAEFFER, D. 2012 The onset of steady vortices in Taylor–Couette flow: the role of approximate symmetry. *Phys. Fluids* **24** (6), 064102.
- COLES, D. 1965 Transition in circular Couette flow. *J. Fluid Mech.* **21** (3), 385–425.
- CROSS, M. C. & HOHENBERG, P. C. 1993 Pattern formation outside of equilibrium. *Rev. Mod. Phys.* **65** (3), 851–1112.
- CZARNY, O., SERRE, E., BONTOUX, P. & LUEPTOW, R. M. 2003 Interaction between Ekman pumping and the centrifugal instability in Taylor–Couette flow. *Phys. Fluids* **15**, 467–477.

- DI PRIMA, R. C. & SWINNEY, H. L. 1981 Instabilities and transition in flow between concentric rotating cylinders. In *Hydrodynamic Instabilities and the Transition to Turbulence*, Topics in Applied Physics, vol. 45, pp. 139–180. Springer.
- EDWARDS, W. S., BEANE, S. R. & VARMA, S. 1991 Onset of wavy vortices in the finite-length Couette–Taylor problem. *Phys. Fluids* **3** (6), 1510–1518.
- GOLUBITSKY, M., STEWART, I. & SCHAEFFER, D. G. 1988 *Singularities and Groups in Bifurcation Theory*, vol. I, Applied Mathematical Sciences, vol. 51. Springer.
- GUCKENHEIMER, J. & HOLMES, P. 1983 *Nonlinear Oscillations, Dynamical Systems, and Bifurcations of Vector Fields*, Applied Mathematical Sciences, vol. 42. Springer.
- HEISE, M., ABSHAGEN, J., HOCHSTRATE, K., KÜTER, D., PFISTER, G. & HOFFMANN, C. 2008 Localized spirals in Taylor–Couette flow. *Phys. Rev. E* **77**, 026202.
- HEISE, M., HOFFMANN, C., WILL, C., ALTMAYER, S., ABSHAGEN, J. & PFISTER, G. 2013 Co-rotating Taylor–Couette flow enclosed by stationary disks. *J. Fluid Mech.* **716**, R4 (12pp).
- HOFFMANN, C., ALTMAYER, S., PINTER, A. & LÜCKE, M. 2009 Transitions between Taylor vortices and spirals via wavy Taylor vortices and wavy spirals. *New J. Phys.* **11**, 053002.
- HOFFMANN, C. & LÜCKE, M. 2000 Spiral vortices and Taylor vortices in the annulus between counter-rotating cylinders. In *Physics of Rotating Fluids*, Lecture Notes in Physics, vol. 549, pp. 55–66. Springer.
- HOFFMANN, C., LÜCKE, M. & PINTER, A. 2004 Spiral vortices and Taylor vortices in the annulus between rotating cylinders and the effect of an axial flow. *Phys. Rev. E* **69** (5), 056309.
- HOFFMANN, C., LÜCKE, M. & PINTER, A. 2005 Spiral vortices travelling between two rotating defects in the Taylor–Couette system. *Phys. Rev. E* **72** (5), 056311.
- LANGFORD, W. F., TAGG, R., KOSTELICH, E. J., SWINNEY, H. L. & GOLUBITSKY, M. 1988 Primary instabilities and bicriticality in flow between counter rotating cylinders. *Phys. Fluids* **31**, 776–785.
- LOPEZ, J. M. & MARQUES, F. 2002 Modulated Taylor–Couette flow: onset of spiral modes. *Theor. Comput. Fluid Dyn.* **16**, 59–69.
- LOPEZ, J. M., MARQUEZ, F. & SHEN, J. 2000 Endwall effects in a periodically forced centrifugally unstable flow. *Fluid Dyn. Res.* **27** (2), 91.
- LORENZEN, A., PFISTER, G. & MULLIN, T. 1983 End effects on the transition to time-dependent motion in the Taylor experiment. *Phys. Fluids* **26** (1), 10–13.
- MARQUES, F. & LOPEZ, J. M. 2000 Spacial and temporal resonances in a periodically forced hydrodynamic system. *Physica D* **136**, 340–352.
- TAGG, R. 1994 The Couette–Taylor problem. *Nonlinear Sci. Today* **4** (3), 1–25.